

Asymmetric Topological Valley Edge States on Silicon-On-Insulator Platform

Hongwei Wang, Lu Sun, Yu He, Guojing Tang, Shaohua An, Zhen Wang, Yuhua Du, Yong Zhang, Luqi Yuan, Xintao He, Jianwen Dong, and Yikai Su*

Valley-Hall photonic topological insulators (VPTIs) provide an intriguing approach to suppress backscattering, enhance the robustness of transport, and shrink the footprints of the topological devices. However, previous works focused on the transmission characteristics of the symmetric topological waveguides with few reports on functional devices involving edge mode coupling, which hinders the implementation of various functional devices such as optical couplers/splitters, switches, filters, and etc. In this paper, a new method to manipulate the mode field distributions in topological waveguides is demonstrated by introducing asymmetric edge states, thus the mode coupling with an arbitrary coupling ratio can be achieved between topological waveguides. As an example, a topological power splitter with a 33:67 splitting ratio is demonstrated experimentally. In addition, to verify the robust transmission property of the topological photonic devices, a high-speed data transmission experiment for a topological power splitter is performed and a high data rate of 128 Gb s^{-1} is achieved. These results promise a new method to manipulate the mode field distribution in topological waveguides and devices that may find wide applications in diverse fields such as optical communications, nanophotonics, and quantum information processing.

1. Introduction


Topology is an important concept in physics nowadays, which has attracted much attention in diverse fields ranging from

H. Wang, L. Sun, Y. He, S. An, Z. Wang, Y. Du, Y. Zhang, Y. Su
State Key Laboratory of Advanced Optical Communication Systems and Networks

Department of Electronic Engineering
Shanghai Jiao Tong University
Shanghai 200240, China
E-mail: yikaisu@sjtu.edu.cn

G. Tang, X. He, J. Dong
State Key Laboratory of Optoelectronic Materials and Technologies &
School of Physics
Sun Yat-sen University
Guangzhou 510275, China

L. Yuan
School of Physics and Astronomy
Shanghai Jiao Tong University
Shanghai 200240, China

 The ORCID identification number(s) for the author(s) of this article can be found under <https://doi.org/10.1002/lpor.202100631>

DOI: 10.1002/lpor.202100631

condensed matter physics^[1–8] to photonics^[9–20] and acoustics.^[21–25] In topological photonic insulators, photons insulate in the bulk, but conduct along the edge.^[11] Therefore, the photonic topological insulators (PTIs) have been considered as a promising platform for studying topologically protected transport of light.^[9,10,17] Normally, PTIs can be implemented by employing a broken^[16,26] or a preserved^[11–13,27,28] time-reversal symmetry (TRS). In particular, PTIs with a preserved TRS (PTRS) exhibit compact footprints and lossless optical transport compared to the broken TRS, thus are much preferred for on-chip applications on dielectric photonic crystal (PhC) platform at telecom frequencies. In previous studies, several optical degrees of freedom have been explored to realize topological photonics with PTRS, including the polarizations in bi-anisotropic metamaterials,^[17] TE and TM modes in PhCs,^[29] chiralities of whispering-gallery modes in ring resonators,^[18] *p*- and *d*-orbitals in artificial photonic atoms^[13] and the valley pseudospin in PhCs.^[11,15,28] Compared with other approaches, the valley photonic crystal (VPC)-based structures are much preferred to construct topological photonic devices due to their low losses, broad bandwidths, and compact footprints.^[11] VPCs can be realized by reducing the lattice symmetry from C_{6v} to C_{3v} , for example, by using honeycomb lattices with a broken symmetry.^[11,15,30–35] It is viable to adjust the dimensions of the honeycomb lattices to construct VPCs with different valley-Chern numbers, where the topological edge can be formed at the interface between two different VPCs.^[11] Based on this theory, topologically protected photonic waveguides,^[11,32] electrically pumped topological laser,^[33] valley-dependent quantum photonic circuits,^[34] and topological channel intersections^[35,36] have been realized for on-chip communications.

However, most previous works were limited to the transmission characteristics of symmetric edge states in waveguides with few reports on functional devices.^[11,28] As an important role in the design of integrated functional devices,^[37] the coupling mechanism in topological photonics is still unclear and the relevant study is missing, which hinders the implementation of various kinds of essential functional devices like optical couplers/splitters, switches, filters, and etc. The mode-coupling the-

ory in topological photonics is highly desired to be explored, since it effectively enables the implementation of future versatile, robust, multi-functional topological photonic circuits.

In this paper, we propose a new method to manipulate the distribution of the mode profile in topological waveguides by introducing asymmetric edge states, which are constructed in non-mirror-symmetric structures based on different VPCs around the edge. The mode profile distributions of the asymmetric topological waveguides can be tuned by changing the parameters of VPCs. The evanescent fields on the left and right sides of the asymmetric edge state have different decaying coefficients. To break the orthogonality between two kinds of asymmetric edge states, a bend structure with a 60° sharp turn is introduced, which assists the mode coupling process. By manipulating the mode profile distributions of the two asymmetric edge states, the field overlap can be adjusted, thus achieving an arbitrary coupling ratio. Then, one can realize a large number of topological functional devices based on asymmetric topological waveguides. To verify the feasibility of the proposed scheme, an on-chip power splitter with a 33:67 splitting ratio is designed and fabricated. Moreover, although all previous studies claimed the unique property of robust transmission for the topological devices, no high-speed transmission experiment has ever been performed at the telecom wavelength. Here, we carry out a high-speed data transmission experiment to study the transmission performance of the proposed TPS. The experimental results show that the power penalty induced by the topological device is less than 1 dB with a high-speed 128 Gb s⁻¹ four-level pulse amplitude modulation (PAM-4) signal. To the best of our knowledge, this is the first demonstration of a high-speed transmission experiment employing the proposed TPS in the telecom band. This work shows the feasibility of utilizing topological properties in VPCs for on-chip applications, such as optical communications, photonic integrated circuits, and quantum information processing.

2. Results

In this work, we propose two photonic-crystal-based valley Hall topological structures based on the silicon-on-insulator (SOI) platform. **Figure 1a** is a band diagram of the PhC slab with C_{6v} symmetry. In **Figure 1b**, a honeycomb-type lattice is adopted to construct the VPC structure with a lattice constant a₀ = 433 nm. The unit cell of the VPC structure consists of two inverted equilateral triangular air holes A and B with side lengths of d₁ and d₂, respectively. We start with a honeycomb lattice with the C_{6v} symmetry (d₁ = d₂), which has a Dirac cone in the momentum space at the K/K' points as shown by the red-dotted curves in **Figure 1a**. By employing asymmetric triangular holes with different dimensions within a unit cell (d₁ ≠ d₂), the spatial-inversion symmetry is broken and an energy bandgap can be observed at the K point, as illustrated by the blue-diamond curve in **Figure 1a**.

In the VPC, the phase distribution of the magnetic field component H_z, i.e., arg(H_z), exhibits opposite chirality at different frequencies since it possesses intrinsic circular-polarized orbital angular momentum (OAM). The OAM term can be characterized by the topological charge $l = \int_L \nabla [\arg(H_z)] d\vec{s} / 2\pi$.^[31] Thus, the H_z field at K point has a right-handed circular polarized (RCP)

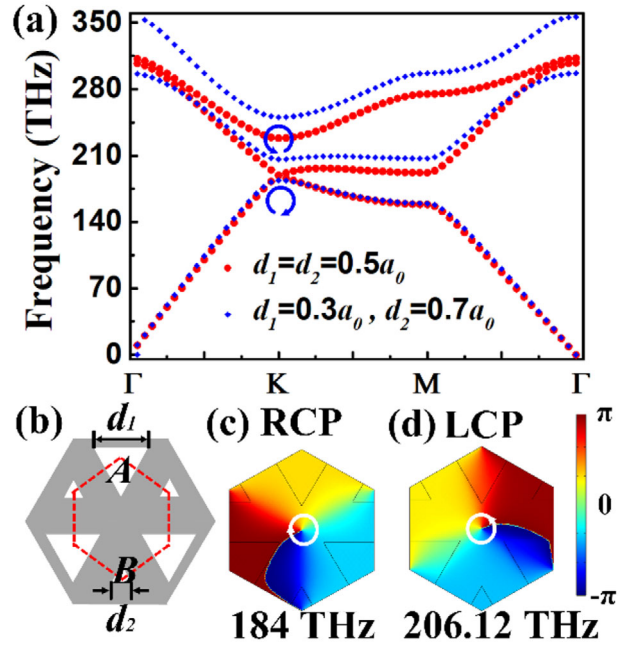


Figure 1. Topological VPC and its bulk band diagram. a) Band diagram of the PhC slab with C_{6v} symmetry (red-dotted curves) compared with C_{3v} symmetry (blue-diamond curves). In the first Brillouin zone, Γ , K, and M denote the high-symmetry points, respectively. b) The dashed hexagon in the schematic presents the unit cell of the VPC slab. The phase distributions of magnetic field component H_z, i.e., arg(H_z), at the frequency of 184 THz in (c), 206.12 THz in (d) for C_{3v} symmetry at the K point as shown in (b).

OAM with $l = 1$ around the central point of the unit cell at the frequency of 189 THz, as shown in **Figure 1c**. On the contrary, for the K valley state at the frequency of 206.12 THz, the H_z phases decrease clockwise instead, thus the H_z field with $l = -1$ can be defined as a left-handed circular polarized (LCP) OAM (**Figure 1d**). With the $k \times p$ perturbation method, the effect of the broken symmetry around the K/K' point can be described by the following Hamiltonian equation (Equation 1):^[11]

$$H_{K/K'} = \tau_z \nu_D (\sigma_x \delta k_x + \sigma_y \delta k_y) + \tau_z \gamma \sigma_z \quad (1)$$

where $\tau_z = 1$ (-1) indicates the K (K') valley pseudospin, ν_D is the group velocity, $\sigma_{x,y,z}$ is the Pauli matrix, and γ denotes the strength of the symmetry-breaking perturbation. Although the band diagrams near the two valleys (K and K') have identical dispersion characteristics, they are topologically distinct. The half-integer valley-Chern number $C_{K/K'} = \tau_z \text{sgn}(\gamma) / 2$ can be obtained by integrating the Berry curvature around the K/K' point.^[28,31]

Figure 2a,b shows the details of two different asymmetric edge states based on the interfaces constructed by two kinds of honeycomb PhCs (VPC₁, VPC₂). In the unit cell of VPC₁ (red dotted curve), the larger and smaller triangular air holes with $a_1 = 0.72a_0$ and $a_2 = 0.28a_0$ point downward (∇) and upward (Δ), respectively. As for the VPC₂, the larger and smaller triangular air holes that construct the lattice (blue dotted curve) point upward (Δ) and downward (∇), respectively, with $b_1 = 0.66a_0$, $b_2 = 0.34a_0$. To explore the coupling mechanism in topological photonics, two

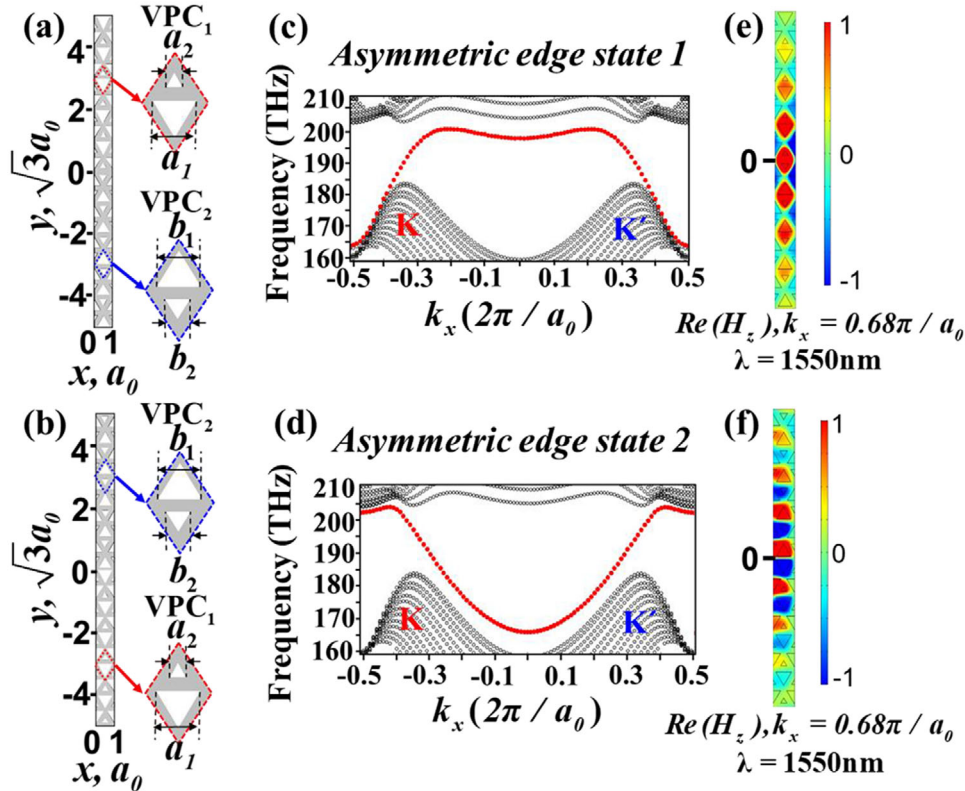


Figure 2. Edge states in the VPC-based topological insulator. a,b) Structures for the asymmetric even-like and odd-like modes in one period along the x direction with gray and white regions representing silicon and air, respectively. c,d) Band diagrams of the two modes showing the edge states (red dotted curve) of the PhCs with $a_1 = 0.72a_0$, $a_2 = 0.28a_0$ and $b_1 = 0.66a_0$, $b_2 = 0.34a_0$, where $a_0 = 433\text{nm}$. e,f) H_z field distributions for the edge states of 2D topological PhCs along the x direction.

edge states are constructed by VPC_1 and VPC_2 . Therefore, the valley Chern number difference between VPC_1 and VPC_2 of the two asymmetric edges are $\Delta C_{\text{edge1}}^{K/K'} = \mp 1$ and $\Delta C_{\text{edge2}}^{K/K'} = \pm 1$, respectively (Note S1, Supporting Information). The band diagrams of the topological edges are shown in Figure 2c,d, respectively. It can be noted that there is a red dotted curve crossing the bandgap between the first and second bulk bands (black dotted curves), which indicates the existence of the edge states for edge 1 and edge 2, respectively. The two curves are both linear at K point and K' point, which means the group velocities of the two asymmetric edge states are constant and of opposite signs. The dispersion curves of the edge states are gapped, which has already been discussed in Ref. [31]. Figure 2e,f indicates that the intensity distributions of the mode profile above and below the edge ($y = 0$) are not the same for the two edge states. The evanescent fields on the left and right sides of the asymmetric edge state have different decay rates in Figure S1 (Supporting Information). The asymmetric edge states 1 and 2 can be regarded as asymmetric even-like and odd-like modes, respectively, in analogy to the mode profiles of the symmetric counterpart, as shown in Figure S4a,b in Note S4 (Supporting Information). Here, the H_z field distributions of two modes are asymmetric with respect to the interface between VPC_1 and VPC_2 , which can be attributed to the different attenuation indices α_1 and α_2 of the even-like eigenstate $|\Psi_{\text{even}}^K\rangle$ induced by the dimension differences of the triangular holes in the top and bottom VPCs ($\alpha_1 > \alpha_2$).

After studying the mode profiles, we further explore the mode coupling scheme for asymmetric edge states, which is essential for on-chip topological devices. In asymmetric topological edges where the overlap coefficient between the odd-like mode and the even-like mode is zero ($\langle \Psi_{\text{even},0}^K | \Psi_{\text{odd},0}^K \rangle = 0$), it is challenging to achieve a high-efficient mode coupling by using a conventional straight topological waveguide (for details, see Note S2, Supporting Information). To enable the mode coupling between different kinds of asymmetric edges, it is necessary to maximize the overlap of the two modes, which can be realized by introducing a bend structure with a sharp turn. The principle can be described as follows: by using a bend structure to break the orthogonality between the odd-like and even-like modes, a rotation operation $\mathfrak{R}(\theta)$ with an angle θ is introduced to increase the mode overlap coefficient, i.e., $\langle \Psi_{\text{even}}^K | \mathfrak{R}(\theta) | \Psi_{\text{odd}}^K \rangle$. The asymmetric even-like mode can be effectively converted into an asymmetric odd-like mode with a nonzero mode coupling efficiency $\eta_{\text{odd},e}^{\theta}$, where θ is chosen as $2\pi/3$ to keep the same valley degree of the two modes. Detailed derivations can be found in Note S2 (Supporting Information). We simulate the light propagation along the interfaces of a 120° and a 60° turn at 1550 nm by using 2D simulations, as shown in Figure 3a,b, respectively. The numerical results prove that the asymmetric even-like mode can be converted into an asymmetric odd-like mode with a 60° turn.

In order to improve the simulation efficiency, the simulation results including the band diagrams, the transmittance, and the

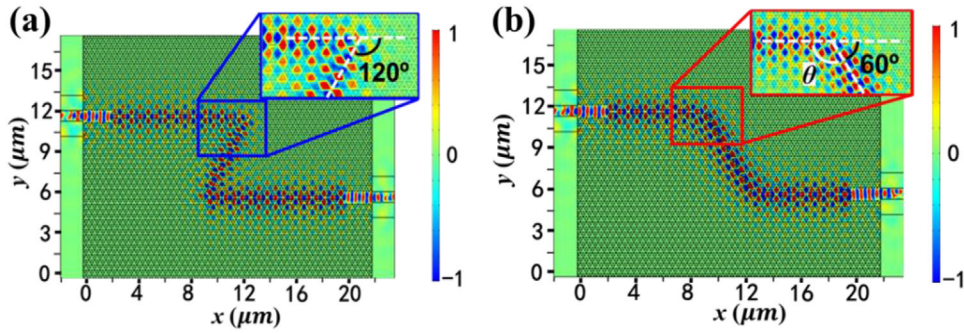


Figure 3. Coupling of different topological modes. a, b) Simulated H_z field distribution of the topological mode coupling at 193 THz ($\lambda = 1550$ nm). The PhCs are both composed of VPC_1 and VPC_2 .

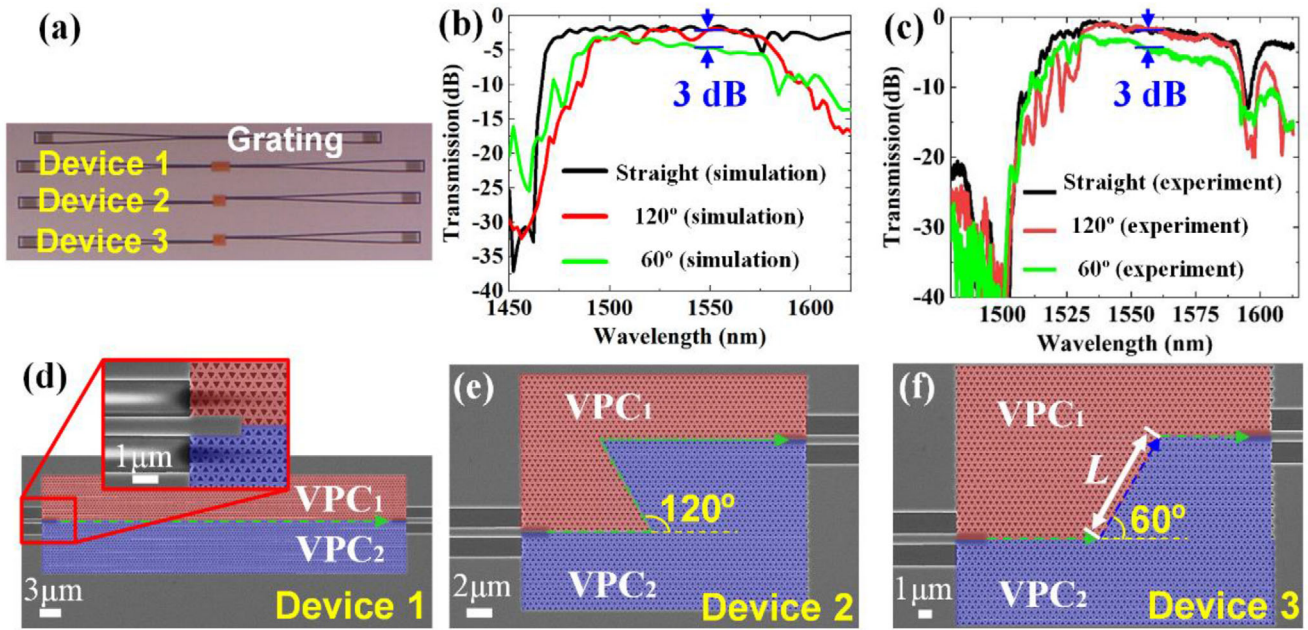


Figure 4. Observation of the asymmetric topological mode coupling based on the silicon VPC. a) Optical microscope photo of the fabricated topological devices. b) Simulated and c) measured transmittances for: the structure with the straight interface (black curve); Z-shaped interface with a 120° turn (red curve); and trapezoid-shaped interface with a 60° turn (green curve). SEM images show the VPC slabs, including devices composed of VPC_1 and VPC_2 separated by a straight interface in d, trapezoidal interfaces with a 120° -degree turn in (e) and a 60° turn in (f). Light propagation paths of the even-like mode and odd-like mode are denoted by green arrow and blue arrow, respectively. The propagation length L of the odd-like mode is $19a_0$.

normalized energy-density in the PhC slab were studied in a 2D configuration using the Finite Element Methods (FEMs). As shown in Figure S3 (Supporting Information), the transmission spectra of the light propagation along the interfaces of a 120° turn and a 60° turn are similar to those along a straight interface, which verifies our theoretical predictions that the propagation of light along the asymmetric edge 1 is topologically protected and the coupling of two different asymmetric topological modes in edges 1 and 2 is viable.

To verify the feasibility of the proposed mode coupling scheme, we calculated the transmission spectra of the topological devices using the full 3D finite-difference time domain (FDTD) method (Lumerical Inc.). Then, the devices were fabricated based on the SOI platform and a transmission experiment was carried out. Detailed fabrication process and the experimental setup can be found in the Note S6 (Supporting Information). Vertical cou-

pling method is employed to couple lights between the optical fibers and the silicon chip. The microscope photos of the topological devices and the grating couplers are shown in Figure 4a. The simulated and measured transmission responses of the fabricated topological devices are detailed in Figure 4b,c, respectively. To characterize the transmission properties of the proposed structure, we fabricated three devices with different interfaces: 1) straight waveguide, 2) trapezoid-shaped interface with a 120° turn, and 3) trapezoid-shaped interface with a 60° turn. The scanning electron microscopy (SEM) images of the topological PhC structures are shown in Figure 4d–f. The lengths of the optical paths are set to be equal for the three devices, which are $28 \mu\text{m}$ in this case, to eliminate excess losses induced by the different lengths of three optical paths. To minimize the scattering losses at the input and output ports, PhC line defect waveguides^[11] are introduced at the interfaces between the silicon nanowire wave-

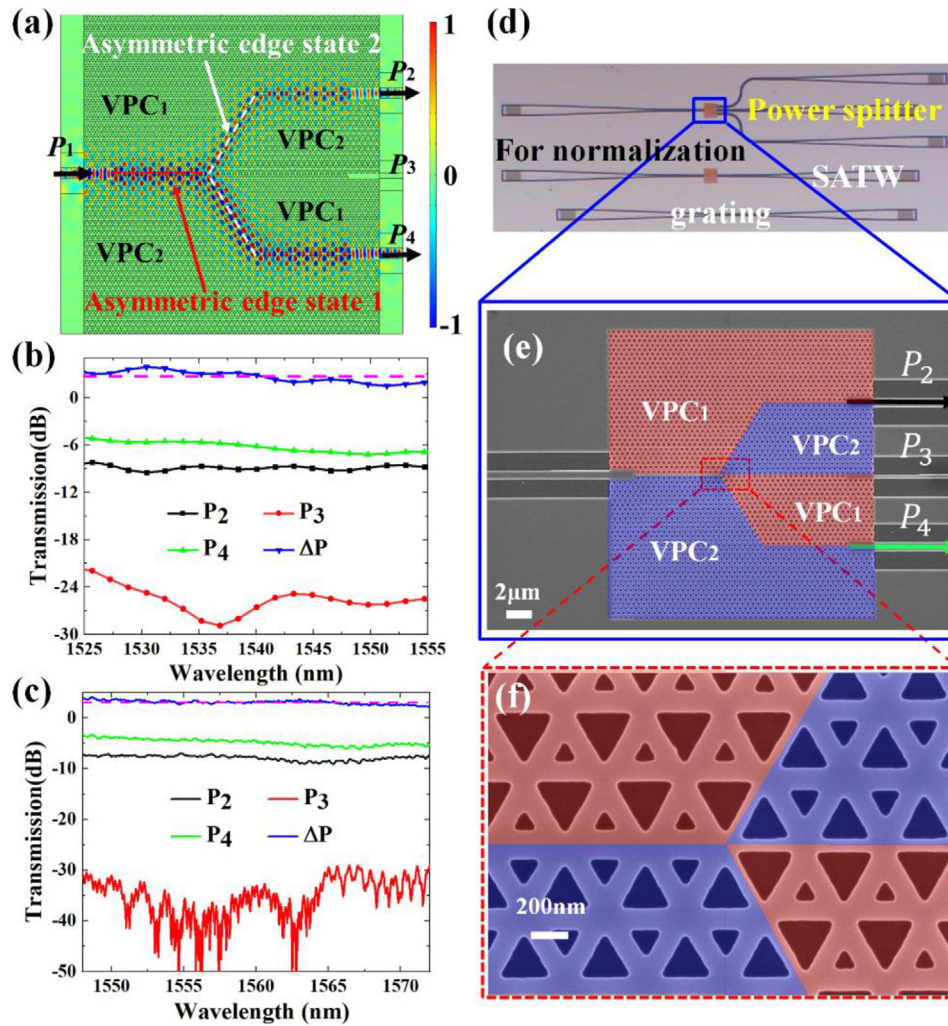


Figure 5. Simulation results and experimental results of the 33:67 TPS. a) Basic structure and simulated H_z field distribution of the 33:67 power splitter working at 193 THz ($\lambda = 1550$ nm). b) Simulated transmission spectra of the 33:67 power splitter. c) Measured transmission spectra of the 33:67 power splitter. d) Optical microscope photo of the 33:67 power splitter. e) SEM images of the fabricated 33:67 power splitter. f) Zoomed-in image showing the joint point of four branches. The sizes of the triangular holes in the PhCs shaded in red and blue are VPC₁ and VPC₂, respectively.

guides and topological devices as the intermediate structures, as shown in the inset of Figure 4d. The width of the silicon nanowire waveguide is 750 nm. We characterize the performance of the devices by using a tunable laser source and an optical power meter. The wavelength of the laser source is swept from 1480 to 1620 nm to measure the transmission responses of the topological devices. Measured transmission responses are normalized to the grating couplers fabricated on the same chip, as plotted in Figure 4c. In the wavelength range of 1530–1575 nm, the insertion losses of devices 1, 2, and 3 are lower than 2.5, 3, and 5.5 dB, respectively, which includes the transmission loss and the coupling loss between the nanowire waveguide, the PhC line defect waveguide and the asymmetric topological waveguide. It can be observed that the measured transmission spectra agree well with the simulation results for the three devices with different interfaces. However, as depicted in Figure 4b,c, there is a 3-dB difference between the transmission loss for device 1 and device 3 in the wavelength range of 1530–1570 nm compared with the 2D simulations as

shown in Note S2 and Figure S3 (Supporting Information). The discrepancy can be attributed to the out-of-plane radiation of the odd-like mode due to its weak confinement of the optical field in a 220-nm-thick silicon slab along the z -direction. The transmission loss of device 3 can be further optimized by decreasing the propagation length (L) of the odd-like mode (for details, see Note S3, (Supporting Information)).

By taking advantage of the demonstrated asymmetric topological even-like-to-odd-like mode coupling method, it is viable to realize a topological photonic power splitter with an arbitrary splitting ratio. As an example, we demonstrate a 1×2 topological photonic power splitter with a splitting ratio of 33:67, as shown in Figure 5a. The principle of the TPS can be explained as follows: the edge states exist at the interfaces between two different VPCs (VPC₁ and VPC₂). The field distributions of different edge states also depend on the size of the triangular holes. By adjusting the dimensions of the triangular holes (a_1 , a_2 , b_1 , b_2 as shown in Figure 2a,b), the modal field distributions can be manipulated. Thus,

it is viable to tune the mode overlap between the two edge states to obtain an arbitrary splitting ratio. The H_z field distribution of our proposed power splitter shows that the light launched from port 1 is transmitted along the asymmetric edge 1, and will be output from ports 2 and 4 with a pre-designed splitting ratio. The light is forbidden to output from port 3 because the even-like-to-odd-like mode coefficient $\eta_{0K \rightarrow eK}$ is zero. The mode coupling coefficients of the even-like mode coupling to the odd-like mode in the upper branch and to the odd-like mode in the lower branch can be written as $\eta_{0K \rightarrow eK}^\uparrow$ and $\eta_{0K \rightarrow eK}^\downarrow$, respectively (superscript “ \uparrow ” and “ \downarrow ” indicate the upper and lower branches). Based on the mode coupling theory, the power splitting ratio ξ can be simplified as:

$\xi = \frac{\eta_{0K \rightarrow eK}^\uparrow}{\eta_{0K \rightarrow eK}^\downarrow} = \frac{\gamma_2^2}{\gamma_1^2} = \frac{(a_2^2 - a_1^2)^2}{(b_2^2 - b_1^2)^2}$. The calculated structural parameters are $a_1 = 0.72a_0$, $a_2 = 0.28a_0$ in VPC₁ and $b_1 = 0.66a_0$, $b_2 = 0.34a_0$ in VPC₂ to achieve a 33:67 power splitting ratio with $\xi = 1/2$ (For details, see Note S5, (Supporting Information)).

The proposed mode coupling theory focuses on the field distribution manipulation along the x - y plane without considering the z -axis. We simulate the performance of the proposed 33:67 power splitter through 3D-FDTD method and the optimized parameters of the triangular holes in the 33:67 power splitter are $a_1 = 334$ nm, $a_2 = 99$ nm, $b_1 = 264$ nm, and $b_2 = 169$ nm, respectively. The simulated imbalance of the power splitting ratio in the 33:67 power splitter is $\approx 3 \pm 1$ dB in the wavelength range of 1525–1555 nm. The simulated and measured transmission spectra of the 33:67 power splitter are plotted in the Figure 5b,c, respectively. A straight asymmetric topological waveguide (SATW) is fabricated on the same wafer for normalization, as shown in Figure 5d. The SEM photos of the fabricated 33:67 power splitter and the coupling region are shown in Figure 5e,f. For the fabricated 33:67 power splitter, the imbalance of the power splitting ratio is $\approx 3 \pm 1$ dB, the measured excess loss is < 3.25 dB at port 2 and the excess loss is < 3.65 dB at port 4 in the wavelength range of 1548–1572 nm. The excess loss of the output ports in TPS can be attributed to the transmission loss of the odd-like mode, which is shown in the Figure 4c.

To pave the way for more applications of topological photonics in optical transmission systems, it is necessary to verify the feasibility of utilizing topological valley-Hall edge states as robust information carriers for on-chip communications. While most previous characterizations are limited to the optical performances, we perform the bit error rate (BER) measurement with a 128 Gb s⁻¹ PAM-4 signal for the TPS in this article. To the best of our knowledge, this is the first demonstration of BER testing with the highest data rate reported in topological devices. Here, we study the transmission performance of a 128 Gb s⁻¹ PAM-4 signal through ports 2 and 4 of TPS at 1550 nm. The experimental setup and transceiver digital signal processing (DSP) flow charts are shown in Figure 6a,b, respectively. The details of the experiment can be found in Section 4. Figure 6c provides the BER curves for ports 2 and 4 in TPS. Compared with the optical back-to-back (OBTB) sensitivity of -9 dBm, a small penalty of 1 dB is observed after the transmission in the TPS. The eye diagrams of the recovered PAM-4 signals at different output ports of the TPS are provided in Figure 6d,e, respectively. The high-speed-transmission experiment unambiguously demonstrates that asymmetric topological modes can be used as carriers for on-chip communication.

3. Discussion

To conclude, we theoretically proposed and experimentally demonstrated a new method to manipulate the mode profile distributions in topological waveguides by introducing asymmetric edge states, and performed a high-speed data transmission experiment of the topological devices at the telecommunication wavelength. The asymmetric topological edges are constructed in non-mirror symmetrical structures based on VPCs. The asymmetric topological even-like mode can be converted to an asymmetric odd-like mode by introducing a bend structure to break the orthogonality between two kinds of asymmetric edge states. By employing the proposed mode coupling method, a large number of functional devices can be realized. As an example, we demonstrate a silicon topological power splitter with a 33:67 splitting ratio. For the proposed TPS, the experimental results show that the imbalance of the power splitting is $\approx 3 \pm 1$ dB in the wavelength range of 1548–1572 nm. Moreover, the high-speed transmission performance based on the TPS is studied, and a low power penalty of < 1 dB is induced by the TPS in a 128 Gb s⁻¹ PAM-4 signal transmission system.

The efficient mode coupling method proposed in this work, combining with standard fabrication techniques, realizes the mode profile manipulation in integrated topological photonics. More applications could be found based on the topological modes, such as topological optical switches, filters, resonant cavities, etc., in the future optical telecommunication and quantum information processing. Furthermore, the high-speed transmission experiment employing our proposed TPS verifies the feasibility of utilizing topological valley-Hall edge states as robust information carriers for on-chip communications, which paves the way for topological photonics applications in practical optical systems.

4. Materials and Methods

Sample Fabrication: The samples^[38] were fabricated and the transmission measurements were performed. The proposed topological devices were fabricated on an SOI wafer (220-nm thick silicon on 3000-nm thick silica). Grating couplers, silicon waveguides, and VPC structures were patterned and etched by e-beam lithography (Vistec EBPG 5200⁺) and inductively coupled plasma etching (SPTS DRIE-I).

Optical Characterization: A tunable continuous wave laser (Keysight 81960A) and an optical power meter (Keysight N7744A) were used to characterize the topological devices. The grating couplers were used to couple the light into/out of the chip. The period and the duty cycle of the grating coupler were 630 nm and 50%, respectively. The etching depth was 70 nm. The coupling loss was 7.5 dB per port at the central wavelengths of the grating coupler. The optical signal was coupled to the silicon chip through the input grating coupler (see Optical characterization setup and fabrication procedure in Note S6, (Supporting Information)). An intermediate waveguide was introduced to connect the conventional waveguide and the topological structure to reduce the mode-wave-vector mismatch and limit scattering to the air. The design of the intermediate waveguide was based on an PhC waveguide with two missing rows of triangular air hole,^[11] as illustrated in the inset of Figure 4d. Then we characterized

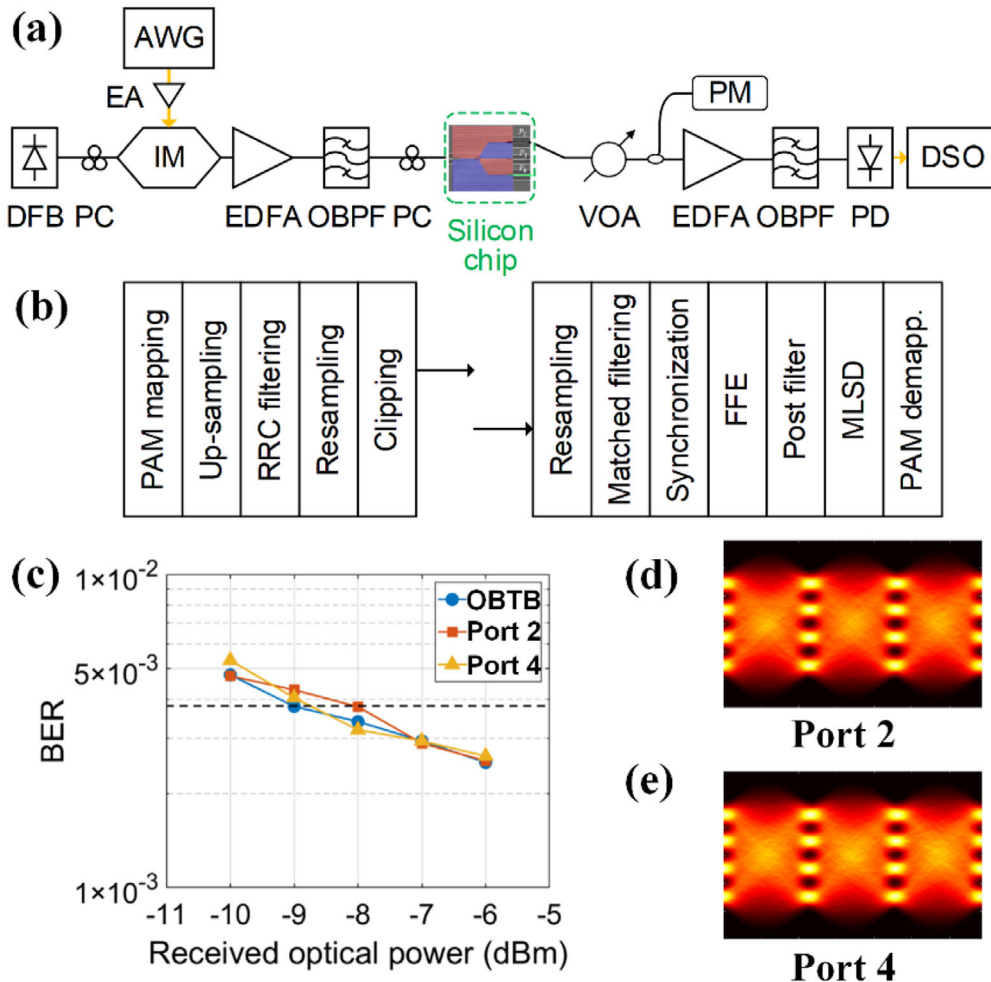


Figure 6. High-speed data transmission experiment based on proposed TPS. a) Experimental setup and b) Digital signal processing (DSP) flow charts for the high data rate transmission. PM, power meter. c) BER curves in different cases. d,e) Eye diagrams at different output ports.

the performances of three devices with different optical paths as shown in Figure 4a, and also fabricated and characterized the power splitter as shown in Figure 5d.

Numerical Simulation: The 2D simulation results, including the band diagrams and the normalized energy-density of the PhC slab (shown in Figures 1, 2, and 5a) were studied by using the FEMs. The effective index of the 220-nm-thick silicon slab was approximated as $n_{eff} = 2.8323$. The transmittance shown in Figures 4b and 5b was calculated with full 3D simulations using Lumerical FDTD Solutions package. The refractive index of silicon was taken as $n_{Si} = 3.48$. The plane wave expansion method was used to calculate the coupling efficiency between two asymmetric topological modes along with theoretical calculations using an effective Dirac Hamiltonian around the K/K' point, as shown in Note S2, (Supporting Information).

High-Speed-Transmission Experimental Setup: The high-speed-transmission experimental setup is shown in Figure 6a,b. At the transmitter side, a PAM-4 symbol sequence was up-sampled and then processed by a root raised cosine (RRC) filter with a roll-off factor of 0.01. After re-sampling and clipping,

the PAM-4 signal was sent to a 65-GSa s^{-1} arbitrary waveform generator (AWG) (Keysight M8195A) and then amplified by an electronic amplifier (EA) to drive a 25-GHz intensity modulator (IM). A continuous wave light from a distributed feedback (DFB) laser was injected into the IM. After electro-optical conversion, the optical PAM-4 signal was boosted by an erbium-doped fiber amplifier (EDFA), and an optical band-pass filter (OBPF) was used to suppress the amplified spontaneous emission noise. The optical signal was then coupled into the silicon chip and transmitted through the topological waveguides. A variable optical attenuator (VOA) was used to adjust the received optical power after the on-chip device. The receiver consisted of an EDFA, an OBPF, a 50-GHz photodetector (PD), and an 80-GSa s^{-1} digital storage oscilloscope (LeCroy 36Zi-A). In the receiver-side DSP, the signal was first resampled to a sampling rate of 128 GSa s^{-1} . After synchronization and matched filtering, a 57-tap linear feedforward equalizer (FFE) was applied. The equalizer coefficients were extracted from the training sequence based on the least mean square (LMS) algorithm. In order to reduce the influence of the noise enhancement effect of the FFE, a

two-tap post filter and maximum likelihood sequence decision (MLSD) were employed. Finally, the PAM-4 demapping and BER calculation were performed.

Supporting Information

Supporting Information is available from the Wiley Online Library or from the author.

Acknowledgements

The work was supported in part by the National Key R&D Program of China under grant 2019YFB2203503 and the National Natural Science Foundation of China (NSFC) (62035016, 61835008, 62105200, 61975115, 61860206001, 11974245). The authors thank the Center for Advanced Electronic Materials and Devices (AEMD) of Shanghai Jiao Tong University (SJTU) for the support in device fabrications. The authors also would like to acknowledge the helpful comments from Jingchi Li and Dahu Feng.

Conflict of Interest

The authors declare no conflict of interest.

Data Availability Statement

The data that support the findings of this study are available in the Supporting Information of this article.

Keywords

asymmetric edge states, topological photonics, valley-Hall photonic topological insulators

Received: November 4, 2021
Revised: February 22, 2022
Published online: March 31, 2022

- [1] X. L. Qi, S. C. Zhang, *Rev. Mod. Phys.* **2011**, *83*, 1057.
[2] M. Z. Hasan, C. L. Kane, *Rev. Mod. Phys.* **2010**, *82*, 3045.
[3] G. Jotzu, M. Messer, R. Desbuquois, M. Lebrat, T. Uehlinger, D. Greif, T. Esslinger, *Nature* **2014**, *515*, 237.
[4] F. Katmis, V. Lauter, F. S. Nogueira, B. A. Assaf, M. E. Jamer, P. Wei, B. Satpati, J. W. Freeland, I. Eremin, D. Heiman, P. Jarillo-Herrero, J. S. Moodera, *Nature* **2016**, *533*, 513.
[5] G. J. Ferreira, D. Loss, *Phys. Rev. Lett.* **2013**, *111*, 106802.
[6] M. C. Diamantini, A. Y. Mironov, S. V. Postolova, X. Liu, Z. Hao, D. M. Silevitch, Y. Kopelevich, P. Kim, C. A. Trugenberger, V. M. Vinokur, *Phys. Lett. A* **2020**, *384*, 23, 126570.
[7] J. E. Moore, *Nature* **2010**, *464*, 194.
[8] C. L. Kane, E. J. Mele, *Phys. Rev. Lett.* **2005**, *95*, 146802.
[9] L. Lu, J. D. Joannopoulos, M. Soljacic, *Nat. Photonics* **2014**, *8*, 821.
[10] T. Ozawa, H. M. Price, A. Amo, N. Goldman, M. Hafezi, L. Lu, M. C. Rechtsman, D. Schuster, J. Simon, O. Zilberberg, I. Carusotto, *Rev. Mod. Phys.* **2019**, *91*, 015006.
[11] M. I. Shalaev, W. Walasik, A. Tsukernik, Y. Xu, N. M. Litchinitser, *Nat. Nanotechnol.* **2019**, *14*, 98.
[12] S. Barik, H. Miyake, W. DeGottardi, E. Waks, M. Hafezi, *New J. Phys.* **2016**, *18*, 113013.
[13] L. H. Wu, X. Hu, *Phys. Rev. Lett.* **2015**, *114*, 223901.
[14] M. C. Rechtsman, J. M. Zeuner, Y. Plotnik, Y. Lumer, D. Podolsky, F. Dreisow, S. Nolte, M. Segev, A. Szameit, *Nature* **2013**, *496*, 196.
[15] T. Ma, G. Shvets, *New J. Phys.* **2016**, *18*, 025012.
[16] K. J. Fang, Z. F. Yu, S. H. Fan, *Nat. Photonics* **2012**, *6*, 782.
[17] A. B. Khanikaev, S. H. Mousavi, W. K. Tse, M. Kargarian, A. H. MacDonald, G. Shvets, *Nat. Mater.* **2013**, *12*, 233.
[18] M. Hafezi, E. A. Demler, M. D. Lukin, J. M. Taylor, *Nat. Phys.* **2011**, *7*, 907.
[19] R. O. Umucalilar, I. Carusotto, *Phys. Rev. A* **2011**, *84*
[20] D. Leykam, L. Yuan, *Nanophotonics* **2020**, *9*, 4473.
[21] J. Y. Lu, C. Y. Qiu, L. P. Ye, X. Y. Fan, M. Z. Ke, F. Zhang, Z. Y. Liu, *Nat. Phys.* **2017**, *13*, 369.
[22] R. Susstrunk, S. D. Huber, *Science* **2015**, *349*, 47.
[23] P. Wang, L. Lu, K. Bertoldi, *Phys. Rev. Lett.* **2015**, *115*, 104302.
[24] V. Peano, C. Brendel, M. Schmidt, F. Marquardt, *Phys. Rev. X* **2015**, *5*, 031011.
[25] Z. J. Yang, F. Gao, X. H. Shi, X. Lin, Z. Gao, Y. D. Chong, B. L. Zhang, *Phys. Rev. Lett.* **2015**, *114*, 114301.
[26] Z. Wang, Y. D. Chong, J. D. Joannopoulos, M. Soljacic, *Nature* **2009**, *461*, 772.
[27] M. I. Shalaev, W. Walasik, N. M. Litchinitser, *Optica* **2019**, *6*, 839.
[28] X. T. He, E. T. Liang, J. J. Yuan, H. Y. Qiu, X. D. Chen, F. L. Zhao, J. W. Dong, *Nat. Commun.* **2019**, *10*, 872.
[29] K. Lai, T. S. Ma, X. Bo, S. Anlage, G. Shvets, *Sci. Rep.* **2016**, *6*.
[30] J. W. Ma, X. Xi, X. K. Sun, *Laser Photonics Rev.* **2019**, *13*, 1900087.
[31] X. D. Chen, F. L. Zhao, M. Chen, J. W. Dong, *Phys. Rev. B* **2017**, *96*, 020202.
[32] Y. Yang, Y. Yamagami, X. Yu, P. Pitchappa, J. Webber, B. Zhang, M. Fujita, T. Nagatsuma, R. Singh, *Nat. Photonics* **2020**, *14*, 446.
[33] Y. Q. Zeng, U. Chattopadhyay, B. F. Zhu, B. Qiang, J. H. Li, Y. H. Jin, L. H. Li, A. G. Davies, E. H. Linfield, B. L. Zhang, Y. D. Chong, Q. J. Wang, *Nature* **2020**, *578*, 246.
[34] Y. Chen, X. T. He, Y. J. Cheng, H. Y. Qiu, L. T. Feng, M. Zhang, D. X. Dai, G. C. Guo, J. W. Dong, X. F. Ren, *Phys. Rev. Lett.* **2021**, *126*, 230503.
[35] L. Zhang, Y. H. Yang, M. J. He, H. X. Wang, Z. J. Yang, E. P. Li, F. Gao, B. L. Zhang, R. Singh, J. H. Jiang, H. S. Chen, *Laser Photonics Rev.* **2019**, *13*.
[36] X. X. Wu, Y. Meng, J. X. Tian, Y. Z. Huang, H. Xiang, D. Z. Han, W. J. Wen, *Nat. Commun.* **2017**, *8*, 1304.
[37] C. Pollock, M. Lipson, *Integrated Photonics*, Kluwer Academic Publishers, Alphen aan den Rijn, the Netherlands **2003**, 301.
[38] Y. K. Su, Y. Zhang, C. Y. Qiu, X. H. Guo, L. Sun, *Adv. Mater. Technol.* **2020**, *5*, 1901153.